Electronic and magnetic properties of Fe-, Co-, and Ni-decorated BC₃: A first-principles study

Jingzhong Zhu [a,b], Yinchang Zhao [c], Muhammad Zulfiqar [a,b], Shuming Zeng [a,b], Jun Ni [a,b,*]

[a] *State Key Laboratory of Low-Dimensional Quantum Physics, Department of Physics, Tsinghua University, Beijing 100084, People's Republic of China*
[b] *Collaborative Innovation Center of Quantum Matter, Beijing 100084, People's Republic of China*
[c] *Department of Physics, Yantai University, Yantai 264005, People's Republic of China*

A B S T R A C T

The electronic and magnetic properties of Fe-, Co-, and Ni-decorated two dimensional (2D) BC₃ are systematically investigated by first-principles calculations. We find that the Fe, Co, and Ni atoms can be strongly adsorbed on the hollow sites of 2D BC₃. Fe and Co adatoms are more stable when adsorbed on the hollow sites of the carbon rings in the 2D BC₃, while the hollow sites of boron-carbon rings in the 2D BC₃ are the most stable sites for the adsorption of Ni adatoms. These proposed metal–BC₃ complexes exhibit interesting electronic and magnetic behaviors. In particular, the Fe–BC₃ and Co–BC₃ complexes are metals with magnetic ground states , while the Ni–BC₃ complex behaves as a nonmagnetic semiconductor with a direct bandgap. Furthermore, our magnetic analysis reveals that induced magnetism in the Fe–BC₃ and Co–BC₃ complexes arises from their local magnetic moments. Functionalization of 2D BC₃ through these metal–adatom adsorption appears to be a promising way to extend its applications.

1. Introduction

Two dimensional materials with a honeycomb structure have attracted much attention in condensed matter physics, chemistry, and materials science [1–10]. Graphene and silicene are typical single-element 2D materials with a honeycomb structure [11–20]. Graphene is a Dirac material and shows a Dirac point in its Fermi energy [21–23]. Silicene shows a buckled structure, which is different from the planar structure of graphene [24–30]. Besides the single-element 2D honeycomb structure materials, compounds with a honeycomb structure consisting of boron, carbon and nitrogen have attracted much attention. In particular, 2D BC₃ with a honeycomb structure has been realized in experiments [31–33]. The 2D BC₃ sheet has been grown epitaxially on the (0001) surface of NbB₂ [34]. The microscopic structure of 2D BC₃ was investigated by scanning tunneling microscope (STM), scanning tunneling spectroscopy (STS) and low energy electron diffraction (LEED) [34]. The 2D BC₃ has a hexagonal crystal structure similar to that of graphene [35]. 2D BC₃ has a bandgap of about 0.54 eV as calculated using local density approximation (LDA) [36].

The tailoring of the electronic structures of 2D BC₃ for their potential applications in designing the hydrogen storage systems is important. Many proposals have already been adopted in this re-

gard [37–41]. The Li-decorated and the Ca-decorated BC₃ sheets can be used for hydrogen storage [42–45] while the Na-decorated BC₃ can be used as methane storage materials [46]. Also, the density-functional theory calculations regarding the polarization, electronic, and magnetic properties of BC₃ sheets decorated with Li, Na, K, and Ca under the application of external electric field have already been reported [47]. Besides alkali metals and alkaline earth metals, transition metals (TM) can also be adopted for chemical functionalization of 2D materials. Transition metals decorated graphene shows exceptionally rich structural, electronic, and magnetic properties [48–55]. However, adsorption of transition metals is not strong enough on graphene. In view of the different chemical activity of boron atoms, we have investigated the electronic and magnetic properties of transition metals decorated BC₃ sheet using first principles calculations.

In this paper, we have systematically investigated the electronic and magnetic properties of Fe-, Co-, and Ni-decorated two dimensional (2D) BC₃ using first-principles calculations. We find that the Fe, Co, and Ni adatoms can be strongly adsorbed on the hollow sites of 2D BC₃. Fe and Co adatoms are more stable when adsorbed on the hollow sites of the carbon rings, while Ni adatom tends to be adsorbed at the hollow sites of boron-carbon rings in the 2D BC₃. These proposed metal–BC₃ complexes exhibit interesting electronic and magnetic behaviors. In particular, the Fe–BC₃ and Co–BC₃ systems exhibit metallic nature with mag-
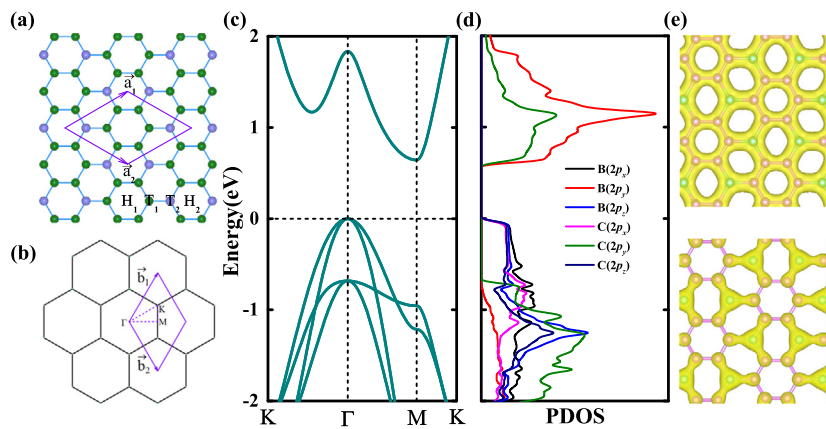
Fig. 1. (Color online.) Electronic structure of the pristine monolayer BC_3. (a) The real space lattices for monolayer BC_3. The purple and green balls represent boron and carbon atoms, respectively. The unit vectors in real space are indicated. (b) The reciprocal space lattice for monolayer BC_3. Γ, K, M are three symmetry points of the first Brillion zone. The three sides (KΓ, ΓM, MK) of the purple triangle are three symmetry lines in the first Brillion zone. The unit vectors in reciprocal space are indicated. (c) The electronic band structure of the pristine monolayer BC_3. (d) The energy dependence of the projected electronic density of states (PDOS) around the valence band top and the conduction band bottom. (e) Partial charge densities of the highest occupied crystal orbital (HOCO) and the lowest unoccupied crystal orbital (LUCO). The Fermi level is set to be zero.

netic ground states, while the Ni–BC_3 system become nonmagnetic direct bandgap semiconductor.

The outline of this paper is as follows: Section 2 describes the calculation methods. In Sec. 3, we show the structures of 2D BC_3 decorated with Fe, Co, and Ni and discuss the electronic and magnetic properties of the system. Section 4 is the summary.

2. Methods

We have performed spin-polarized density functional theory (DFT) calculations implemented in the Vienna ab initio simulation package (VASP) [56,57]. We adopted the projector-augmented wave (PAW) potentials to model the core electrons. We have used a plane wave basis set with an energy cutoff of 500 eV to model the valance electrons. For exchange and correlation, we use the generalized gradient approximation (GGA) of Perdew, Burke, and Ernzernhof (PBE) [58]. A 2×2 BC_3 supercell including 32 nonmetal atoms and an adsorbed transition metal atom is employed. The vacuum region between adjacent BC_3 layers is larger than 15 Å. The Brillouin zone (BZ) sampling is obtained using a $6 \times 6 \times 1$ Monkhorst–Pack grid for relaxation calculations and a $9 \times 9 \times 1$ Monkhorst–Pack grid for static calculations [59]. The tolerance of the energy convergence is 10^{-5} eV. We relax all the structures until the force on each atom is smaller than 0.01 eV/Å.

A 2×2 supercell is adopted in our calculations. The distance between the adjacent adatoms is about 1 nm, which is large enough to avoid interactions between the adjacent adatoms. The binding energies E_b, calculated as a difference between the TM-BC_3 and the energy of the BC_3 plus energy of the isolated atom. We calculated the properties of the BC_3 decorated with Fe, Co and Ni in different supercell: in the case of a 2×2 supercell, the binding energy of H_1 Fe–BC_3, H_1 Co–BC_3 and H_2 Ni–BC_3 are -3.08 eV, -3.25 eV, -3.01 eV, respectively; in the case of a 3×3 supercell, the binding energy of H_1 Fe–BC_3, H_1 Co–BC_3 and H_2 Ni–BC_3 are -3.09 eV, -3.18 eV, -3.02 eV, respectively; in the case of a 4×4 supercell, the binding energy of H_1 Fe–BC_3, H_1 Co–BC_3 and H_2 Ni–BC_3 are -3.10 eV, -3.17 eV, -3.01 eV, respectively. From the point view of binding energy, the results are well convergent. Especially, for the larger 4×4 supercell, the net magnetic moments of H_1 Fe–BC_3, H_1 Co–BC_3 and H_2 Ni–BC_3 are 2 μ_B, 1 μ_B and 0 μ_B, respectively, which are in accordance with those (2 μ_B, 1 μ_B and 0 μ_B) of the 2×2 supercell.

3. Results and discussions

Similar to graphene, 2D BC_3 has a honeycomb structure. The 2D BC_3 shows planar configuration without buckling. A primitive cell of the 2D BC_3 has two boron (B) atoms and six carbon (C) atoms, as depicted in Fig. 1(a). The C–C and B–C bond lengths are 1.42 Å and 1.57 Å, respectively. In the electronic band structure, there is an indirect bandgap of 0.643 eV between the valence band maximum (VBM) located at the Γ point and the conduction band minimum (CBM) located at the M point [shown in Fig. 1(c)], which agrees well with the previous studies [42–44,47]. The analysis of energy dependence of the projected electronic density of states (PDOS) indicates that the $2p_x$ and $2p_z$ orbitals of B atoms and C atoms provides major contribution near VBM, while the main contribution comes from the $2p_y$ orbitals of B and C atoms near CBM. The partial charge densities of the highest occupied crystal orbital (HOCO) and the lowest unoccupied crystal orbital (LUCO) of the pristine monolayer BC_3 are shown in Fig. 1(e). The partial charge densities have the C_{3v} symmetry with a boron atom as the center of the threefold rotational axis which is perpendicular to 2D BC_3 plane.

We first consider a single Fe atom adsorption on the 2×2 BC_3 unit cell. The distance between Fe–Fe in the supercell is about 1 nm so that the interactions between the neighboring Fe atoms could be ignored. Six possible adsorption sites are available on the monolayer BC_3 i.e. two hollow sites (H_1 and H_2), two top sites (T_1 and T_2) and two bridge sites (B_1 and B_2). More precisely, B_1 and B_2 represent the C–C and B–C bridges, respectively. Our calculations indicate that the two bridge sites (B_1 and B_2) are not suitable for the adsorption of Fe, Co and Ni atoms. To be more specific, the configurations with Fe atoms initially residing on the B_1 and B_2 sites are not stable at all and the atoms move to the H_1 and H_2 sites, respectively, after structure relaxation. Similar structural variation is observed for the Co and Ni atoms as well because the Co atoms lying on the B_1 and B_2 sites move to the H_2 and H_1 sites, whereas Ni atoms relocate from the B_1 and B_2 sites to the H_2 and T_1 sites, respectively, after structural relaxation. These four possible stable adsorption sites (H_1, H_2, T_1 and T_2) are depicted in Fig. 1(a). However, the configurations with Fe and Co atoms on the T_1 sites are not stable and the atoms move to the H_1 sites after relaxation. The most stable adsorption sites for Fe–BC_3, Co–BC_3 and Ni–BC_3 are H_1, H_1 and H_2, respectively. The optimized structure of transition-metal-decorated 2D BC_3 with transition-metal-atoms in the most stable adsorption sites are shown in Fig. 2. The bind-
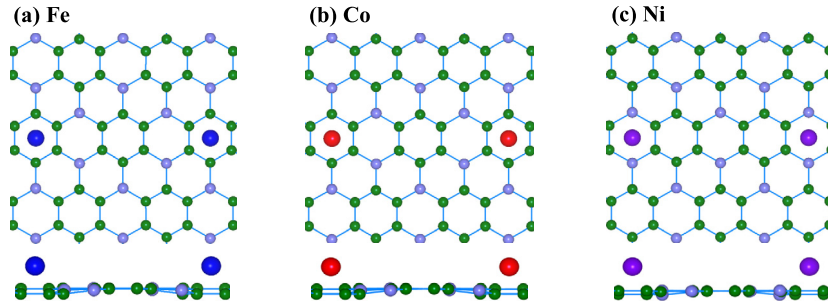
(a) Fe   **(b) Co**   **(c) Ni**

Fig. 2. (Color online.) The optimized structure of transition-metal-decorated 2D BC_3 with transition-metal-atoms in the most stable adsorption sites. Top view and side view of (a) Fe-, (b) Co- and (c) Ni-decorated 2D BC_3, respectively.
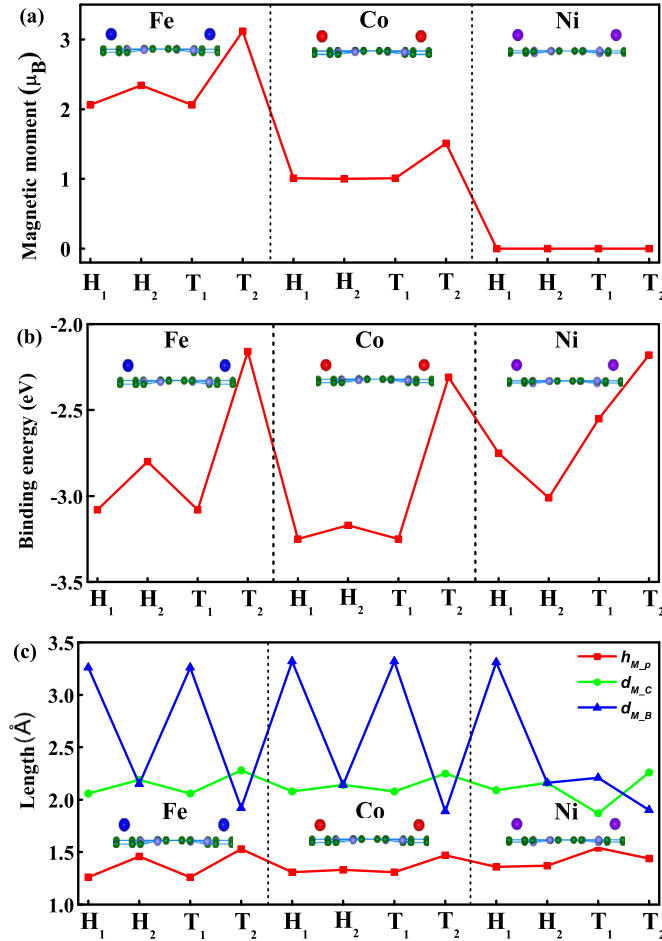

Fig. 3. (Color online.) Magnetic, energy and structural properties of the Fe-, Co-, and Ni-decorated BC_3 sheet. (a) The magnetic moment, (b) the binding energy and (c) the height of the transition atoms over the BC_3 plane (h_{M-P}), the metal–carbon bond length (d_{M-C}), the metal–boron bond length (d_{M-B}). The results of the Fe and Co atoms on the T_1 sites should be considered as those of the Fe and Co atoms on the H_1 sites because the Fe and Co atoms on the T_1 sites are not stable and the atoms move to H_1 sites after relaxation.

ing energy is defined as $E_b = E_d - E_0 - E_m$, where E_d and E_0 are the energies with and without transition metal atoms adsorbed, respectively, and E_m is the energy of a free transition metal atom.

We find that the Fe- and Co-decorated BC_3 sheets are magnetic while the Ni-decorated BC_3 sheet is nonmagnetic, as shown in Fig. 3(a). The energy differences between the ferromagnetic state and nonmagnetic one for the Fe–BC_3 and Co–BC_3 are -0.710 eV and -0.346 eV per supercell (containing 8 B atoms and 24 C atoms), respectively. The magnetic moment of Fe–BC_3 is about 2.0 μ_B when the Fe atoms are adsorbed in the most stable adsorption sites H_1. The magnetic moment of Fe–BC_3 is larger than 2.0 μ_B when the Fe atoms are on the H_2 and T_2 sites. However,

the configurations with the Fe atoms on the H_2 and T_2 sites are less stable than the configurations with the Fe atoms on the H_1 sites. The Co–BC_3 sheet has a magnetic moment of about 1.0 μ_B when the Co atoms are adsorbed in the most stable adsorption sites H_1. The magnetic moment is also 1.0 μ_B when the Co atoms are on the H_2 sites. The binding energy of the H_1 Co–BC_3 is a little smaller than that of the H_2 Co–BC_3, as depicted in Fig. 3(b).

In spite of that the Ni–BC_3 is nonmagnetic whatever the adsorption sites is chosen for the Ni atoms. The binding energy is smallest for Ni–BC_3 when the Ni atom is placed on the H_2 sites, which is different from the most stable H_1 adsorption sites of Fe–BC_3 and Co–BC_3 sheets. The results of the Fe and Co atoms
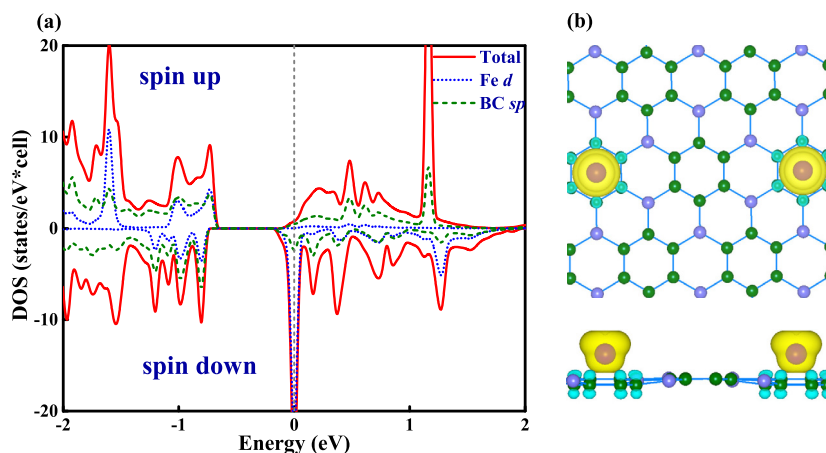
Fig. 4. (Color online.) (a) Spin-up and spin-down total DOS, PDOS on the BC$_3$ sheet, and PDOS on the Fe atom d states for Fe atoms on the H$_1$ sites of BC$_3$. The Fermi energy is set to be zero. (b) The top and side view of spatial spin charge density distributions of Fe atoms on the H$_1$ sites of BC$_3$.

Fig. 5. (Color online.) (a) Spin-polarized total DOS, PDOS on the BC$_3$ sheet, and PDOS on the Co atom d states for Co atoms on the H$_1$ sites of BC$_3$. The Fermi energy is set to be zero. (b) The top and side view of spatial spin charge density distributions of Co atoms on the H$_1$ sites of BC$_3$.
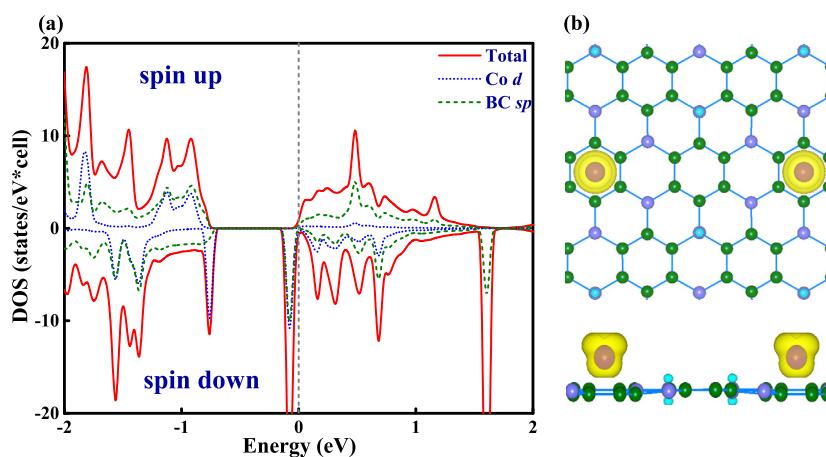
on the T$_1$ sites should be considered as those of the Fe and Co atoms on the H$_1$ sites because the Fe and Co atoms on the T$_1$ sites are not stable, making the atoms to relocate to the H$_1$ sites after structural relaxation. The typical values of binding energies are about −3 eV. The binding energies of H$_1$ Fe–BC$_3$, H$_1$ Co–BC$_3$ and H$_2$ Ni–BC$_3$ are −3.08 eV, −3.25 eV, −3.01 eV, respectively.

The metal adatoms we used have larger binding energies on BC$_3$ sheet as compared with those on graphene surface [52]. To explain qualitatively, we have performed the Bader analysis for all considered systems. Fe, Co, Ni on BC$_3$ have the net charges of about 0.82e, 0.71e, 0.53e, respectively, which are larger than the net charges (0.43e, 0.38e, 0.45e) of Fe, Co, Ni on graphene [52]. Qualitatively, the binding energy increases with the increase of net charge of the adatoms, thus the metal adatoms have larger binding energies on BC$_3$ sheet as compared with those on graphene surface. Secondly, the heights of Fe, Co, Ni on BC$_3$ are about 1.26 Å, 1.31 Å, 1.37 Å, respectively, which are smaller than the heights (1.53 Å, 1.50 Å, 1.54 Å) of Fe, Co, Ni on graphene [52]. Qualitatively, the binding energy increases with the decrease of the heights of the adatoms, thus the metal adatoms have larger binding energies on BC$_3$ sheet as compared with those on graphene surface [52].

The adatom adsorption heights for H$_1$ Fe–BC$_3$, H$_1$ Co–BC$_3$ and H$_2$ Ni–BC$_3$ are 1.26 Å, 1.31 Å and 1.37 Å, respectively, as shown in Fig. 3(c). The typical lengths between the metal atoms and the nearest carbon atoms (d$_{M-C}$) are about 2.0 Å. It is important to mention that the lengths between the metal atoms and the nearest boron atoms (d$_{M-B}$) simply depend upon the chosen adsorption

sites. The typical lengths are 3.3 Å and 2.1 Å for H$_1$ and H$_2$ sites, respectively.

To give a deeper insight regarding the induced magnetism for the H$_1$ Fe–BC$_3$ and H$_1$ Co–BC$_3$, we have utilized the spin-polarized density of states (DOS) of H$_1$ Fe–BC$_3$, H$_1$ Co–BC$_3$ as shown in Figs. 4 and 5, respectively. Fig. 4 shows that the H$_1$ Fe–BC$_3$ DOS near the Fermi energy along with the projection of the DOS onto BC$_3$ and the Fe d states. The most obvious peak is at the Fermi level and it stems from the spin-down d orbitals of Fe. The other two peaks are at about −1.6 eV and 1.3 eV, respectively. The spatial spin charge density distribution of the H$_1$ Fe–BC$_3$ is depicted in Fig. 4(b). It clearly shows that the magnetism in the case of the H$_1$ Fe–BC$_3$ mainly originates due to Fe atoms. Similarly, the magnetism induced in the case of the H$_1$ Co–BC$_3$ mainly stems from Co atoms, as shown in the spatial spin charge density distribution of the H$_1$ Co–BC$_3$ in Fig. 5(b). Fig. 5(a) shows the spin polarized total DOS, PDOS of the BC$_3$ sheet, and PDOS of the d state of the Co atom for the H$_1$ Co–BC$_3$. The most obvious peak lies just below the Fermi level and it comes from the spin-down d orbitals of Co atoms.

The magnetic moments of the isolated Fe, Co, Ni atom are 4 μ_B, 3 μ_B and 2 μ_B, respectively. The H$_1$ Fe–BC$_3$, H$_1$ Co–BC$_3$ and H$_2$ Ni–BC$_3$ show 2 μ_B, 1 μ_B and 0 μ_B magnetic moment, respectively. The reduction of the magnetic moments for Fe, Co and Ni are all 2 μ_B. The charge transfer is intimately connected to the local magnetic moment variation. It can be understood that the spin component (4s ↑) in the isolated atom becomes the minority
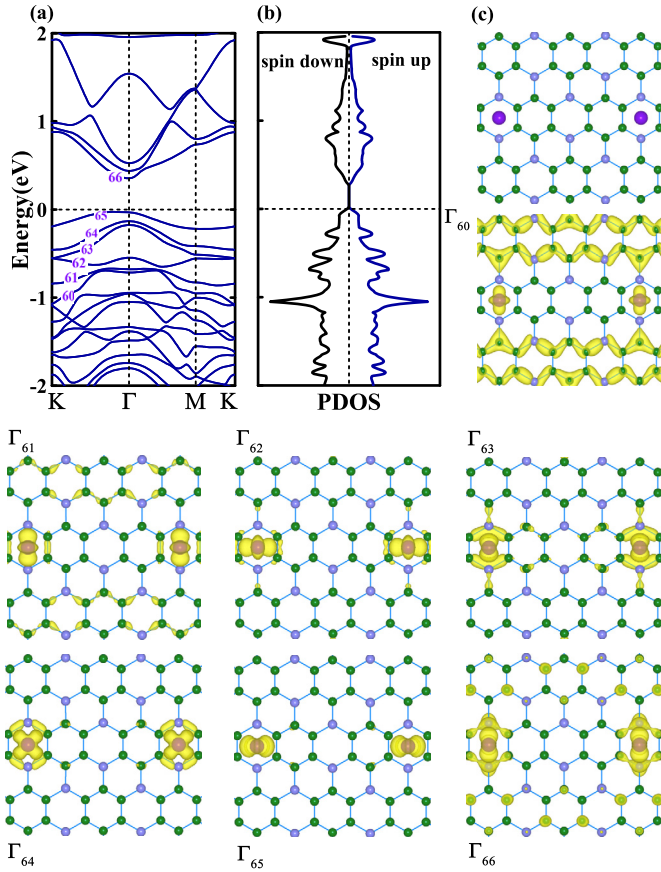
Fig. 6. (Color online.) Electronic structure of the Ni atoms on the H_2 sites of BC_3. (a) The electronic band structure of the Ni atoms on the H_2 sites of BC_3. (b) The energy dependence of the spin polarized electronic density of states around the valence band top and the conduction band bottom. (c) Partial charge densities of some occupied crystal orbital and the lowest unoccupied crystal orbital. The Fermi level is set to be zero.

component (3d ↓) in the TM-BC_3, which causes the reduction of the magnetic moments for Fe, Co and Ni to be all 2 μ_B.

The calculated spin polarized band structure for the Ni adatom residing on the H_2 sites of the BC_3 sheet are depicted in Fig. 6. Some flat electronic impurity bands appear just below the Fermi energy of the H_2 Ni–BC_3. To elaborate the spatial distribution of the electrons due to which these flat impurity bands arises, we have shown the partial charge densities of some highest occupied orbitals and the lowest unoccupied orbitals in Fig. 6(c). Also, the spin polarized electronic density of states (Fig. 6(b)) supports this nonmagnetic characteristics of the H_2 Ni–BC_3. The band gap of H_2 Ni–BC_3 is about 0.38 eV, which is smaller than the band gap of the pristine BC_3 sheet.

It is interesting to compare the electronic and magnetic properties between the adsorbed and the doped BC_3 with Fe, Co and Ni [60]. The adsorption on the H_1 site for Fe–BC_3 and Co–BC_3 leads to metallic feature, whereas the Ni–BC_3 with the H_2 site adsorption exhibits the semiconducting nature. For the doped BC_3, the substitution of Ni for B leads to a semiconductor–metal transition, whereas the other systems maintain the semiconducting nature as that of pristine 2D BC_3 [60]. With H_1 adsorption site, the net magnetic moment of 2 μ_B and 1 μ_B is induced for the Fe–BC_3 and Co–BC_3 sheets, respectively, whereas if the H_2 site is chosen for adsorption, the Ni–BC_3 sheet becomes to nonmagnetic. For the doped BC_3, the substitution of Fe for B or substitution of Co for C induces the net magnetic moments of 1 μ_B in the BC_3 honeycomb structure, whereas the other systems are nonmagnetic [60]. The adsorption or substitution of Fe, Co and Ni may lead to

semiconductor–metal transitions or induce net magnetic moments in the BC_3 honeycomb structure [60].

4. Conclusion

We have studied the electronic and magnetic features of Fe-, Co-, and Ni-decorated BC_3 by first-principles calculations. The Fe and Co atoms can be strongly adsorbed on the hollow sites of the carbon rings, while the Ni atom tends to reside on the hollow sites of the C–N rings. The H_1 Fe–BC_3 and H_1 Co–BC_3 show 2 μ_B and 1 μ_B magnetic moment, respectively. The H_2 Ni–BC_3 is nonmagnetic. BC_3 transforms from insulator to metallic states after the adsorption of Fe or Co atoms. However, the BC_3 keep its insulator state after the adsorption of Ni atoms. The band gap of the BC_3 honeycomb structure becomes smaller after the adsorption of Ni atoms. Functionalization of 2D BC_3 through these metal–adatom adsorption appears to be a promising way to extend its applications.

References

[1] T. Ando, A.B. Fowler, F. Stern, Electronic properties of two-dimensional systems, Rev. Mod. Phys. 54 (1982) 437.
[2] K. Novoselov, Nobel lecture: graphene: materials in the flatland, Rev. Mod. Phys. 83 (2011) 837.
[3] G. Labaigt, A. Dubois, J. Hansen, Electron capture imaging of two-dimensional materials, Phys. Rev. B 89 (2014) 245438.
[4] J. Jung, A. Raoux, Z. Qiao, A.H. MacDonald, Ab initio theory of Moiré superlattice bands in layered two-dimensional materials, Phys. Rev. B 89 (2014) 205414.
[5] D. Wang, D. Han, X.-B. Li, S.-Y. Xie, N.-K. Chen, W.Q. Tian, D. West, H.-B. Sun, S. Zhang, Determination of formation and ionization energies of charged defects in two-dimensional materials, Phys. Rev. Lett. 114 (2015) 196801.
[6] L.H. Tizei, Y.-C. Lin, M. Mukai, H. Sawada, A.-Y. Lu, L.-J. Li, K. Kimoto, K. Suenaga, Exciton mapping at subwavelength scales in two-dimensional materials, Phys. Rev. Lett. 114 (2015) 107601.
[7] P. Cudazzo, L. Sponza, C. Giorgetti, L. Reining, F. Sottile, M. Gatti, Exciton band structure in two-dimensional materials, Phys. Rev. Lett. 116 (2016) 066803.
[8] B.C. McGuigan, P. Pochet, H.T. Johnson, Critical thickness for interface misfit dislocation formation in two-dimensional materials, Phys. Rev. B 93 (2016) 214103.
[9] L. Seixas, A. Rodin, A. Carvalho, A.C. Neto, Multiferroic two-dimensional materials, Phys. Rev. Lett. 116 (2016) 206803.
[10] R. Haleoot, C. Paillard, T.P. Kaloni, M. Mehboudi, B. Xu, L. Bellaiche, S. Barraza-Lopez, Photostrictive two-dimensional materials in the monochalcogenide family, Phys. Rev. Lett. 118 (2017) 227401.
[11] C.L. Kane, E.J. Mele, Quantum spin hall effect in graphene, Phys. Rev. Lett. 95 (2005) 226801.
[12] A.C. Ferrari, J. Meyer, V. Scardaci, C. Casiraghi, M. Lazzeri, F. Mauri, S. Piscanec, D. Jiang, K. Novoselov, S. Roth, et al., Raman spectrum of graphene and graphene layers, Phys. Rev. Lett. 97 (2006) 187401.
[13] Y.-W. Son, M.L. Cohen, S.G. Louie, Energy gaps in graphene nanoribbons, Phys. Rev. Lett. 97 (2006) 216803.
[14] Q. Yan, B. Huang, J. Yu, F. Zheng, J. Zang, J. Wu, B.-L. Gu, F. Liu, W. Duan, Intrinsic current-voltage characteristics of graphene nanoribbon transistors and effect of edge doping, Nano Lett. 7 (2007) 1469–1473.
[15] Y. Yao, F. Ye, X.-L. Qi, S.-C. Zhang, Z. Fang, Spin-orbit gap of graphene: first-principles calculations, Phys. Rev. B 75 (2007) 041401.
[16] Z. Li, H. Qian, J. Wu, B.-L. Gu, W. Duan, Role of symmetry in the transport properties of graphene nanoribbons under bias, Phys. Rev. Lett. 100 (2008) 206802.
[17] B. Huang, Z. Li, Z. Liu, G. Zhou, S. Hao, J. Wu, B.-L. Gu, W. Duan, Adsorption of gas molecules on graphene nanoribbons and its implication for nanoscale molecule sensor, J. Phys. Chem. C 112 (2008) 13442–13446.
[18] X. Dong, Y. Shi, Y. Zhao, D. Chen, J. Ye, Y. Yao, F. Gao, Z. Ni, T. Yu, Z. Shen, et al., Symmetry breaking of graphene monolayers by molecular decoration, Phys. Rev. Lett. 102 (2009) 135501.

[19] A.C. Neto, F. Guinea, N.M. Peres, K.S. Novoselov, A.K. Geim, The electronic properties of graphene, Rev. Mod. Phys. 81 (2009) 109.

[20] C.-C. Liu, W. Feng, Y. Yao, Quantum spin hall effect in silicene and two-dimensional germanium, Phys. Rev. Lett. 107 (2011) 076802.

[21] L. Dell'Anna, A. De Martino, Magnetic superlattice and finite-energy Dirac points in graphene, Phys. Rev. B 83 (2011) 155449.

[22] A. Rahman, J.W. Guikema, N. Marković, Quantum interference noise near the Dirac point in graphene, Phys. Rev. B 89 (2014) 235407.

[23] J.H. Bardarson, J. Tworzydło, P. Brouwer, C. Beenakker, One-parameter scaling at the Dirac point in graphene, Phys. Rev. Lett. 99 (2007) 106801.

[24] X. Lin, J. Ni, Much stronger binding of metal adatoms to silicene than to graphene: a first-principles study, Phys. Rev. B 86 (2012) 075440.

[25] W. Li, S. Sheng, J. Chen, P. Cheng, L. Chen, K. Wu, Ordered chlorinated monolayer silicene structures, Phys. Rev. B 93 (2016) 155410.

[26] J. Qiu, H. Fu, Y. Xu, A. Oreshkin, T. Shao, H. Li, S. Meng, L. Chen, K. Wu, Ordered and reversible hydrogenation of silicene, Phys. Rev. Lett. 114 (2015) 126101.

[27] H. Wu, Y. Qian, Z. Du, R. Zhu, E. Kan, K. Deng, Prediction of another semimetallic silicene allotrope with Dirac fermions, Phys. Lett. A 381 (2017) 3754–3759.

[28] Y.-L. Sun, C. Zhu, J. Chen, E.-J. Ye, Dynamic conductance in double-bend silicene nanosystem, Phys. Lett. A 381 (2017) 2699–2703.

[29] S. Alesheikh, N. Shahtahmassebi, M.R. Roknabadi, R.P. Shahri, Silicene nanoribbon as a new DNA sequencing device, Phys. Lett. A 382 (8) (2018) 595–600.

[30] C.-C. Liu, H. Jiang, Y. Yao, Low-energy effective hamiltonian involving spin-orbit coupling in silicene and two-dimensional germanium and tin, Phys. Rev. B 84 (2011) 195430.

[31] K.M. Krishnan, Structure of newly synthesized BC$_3$ films, Appl. Phys. Lett. 58 (1991) 1857–1859.

[32] H. Yanagisawa, T. Tanaka, Y. Ishida, E. Rokuta, S. Otani, C. Oshima, Phonon dispersion curves of stable and metastable BC$_3$ honeycomb epitaxial sheets and their chemical bonding: experiment and theory, Phys. Rev. B 73 (2006) 045412.

[33] Z. Weng-Sieh, K. Cherrey, N.G. Chopra, X. Blase, Y. Miyamoto, A. Rubio, M.L. Cohen, S.G. Louie, A. Zettl, R. Gronsky, Synthesis of B$_x$C$_y$N$_z$ nanotubules, Phys. Rev. B 51 (1995) 11229.

[34] A. Ueno, T. Fujita, M. Matsue, H. Yanagisawa, C. Oshima, F. Patthey, H.-C. Ploigt, W.-D. Schneider, S. Otani, Scanning tunneling microscopy study on a BC$_3$ covered nbb 2 (0001) surface, Surf. Sci. 600 (2006) 3518–3521.

[35] S.-Y. Liu, S. Liu, D.-J. Li, H. Dang, Y. Liu, S. Xue, W. Xue, S. Wang, Bonding, stability, and electronic properties of the BC$_3$ honeycomb monolayer structure on nbb 2 (0001), Phys. Rev. B 88 (2013) 115434.

[36] Y. Ding, Y. Wang, J. Ni, Electronic structures of BC$_3$ nanoribbons, Appl. Phys. Lett. 94 (2009) 073111.

[37] M. Moradi, A.A. Peyghan, Role of sodium decoration on the methane storage properties of BC$_3$ nanosheet, Struct. Chem. 25 (2014) 1083–1090.

[38] F.J. Ribeiro, M.L. Cohen, Possible superconductivity in hole-doped BC$_3$, Phys. Rev. B 69 (2004) 212507.

[39] H. Yanagisawa, T. Tanaka, Y. Ishida, M. Matsue, E. Rokuta, S. Otani, C. Oshima, Phonon dispersion curves of a BC$_3$ honeycomb epitaxial sheet, Phys. Rev. Lett. 93 (2004) 177003.

[40] X. Chen, J. Ni, Fermi surface nesting and magnetic quantum phase transition in graphenelike BC$_3$: a first-principles study, Phys. Rev. B 88 (2013) 115430.

[41] X. Chen, Y. Yao, H. Yao, F. Yang, J. Ni, Topological p + ip superconductivity in doped graphene-like single-sheet materials BC$_3$, Phys. Rev. B 92 (2015) 174503.

[42] Z. Yang, J. Ni, Hydrogen storage on calcium-decorated BC$_3$ sheet: a first principles study, Appl. Phys. Lett. 97 (2010) 253117.

[43] Z. Yang, J. Ni, Li-doped BC$_3$ sheet for high-capacity hydrogen storage, Appl. Phys. Lett. 100 (2012) 183109.

[44] Y. Zhang, X. Cheng, Hydrogen storage on Li coated BC$_3$ honeycomb sheet, Chin. J. Chem. (2017).

[45] A.A. Kuzubov, A.S. Fedorov, N.S. Eliseeva, F.N. Tomilin, P.V. Avramov, D.G. Fedorov, High-capacity electrode material BC$_3$ for lithium batteries proposed by ab initio simulations, Phys. Rev. B 85 (2012) 195415.

[46] M. Moradi, A.A. Peyghan, Role of sodium decoration on the methane storage properties of BC$_3$ nanosheet, Struct. Chem. 25 (2014) 1083–1090.

[47] Y. Zhao, M. Zulfiqar, J. Ni, Strong coupling between magnetization and electric polarization in BC$_3$ sheet adsorbed with Li, Na, K, and Ca, Solid State Commun. 226 (2016) 13–18.

[48] A. Bhattacharya, S. Bhattacharya, C. Majumder, G. Das, Transition-metal decoration enhanced room-temperature hydrogen storage in a defect-modulated graphene sheet, J. Phys. Chem. C 114 (2010) 10297–10301.

[49] H. Lee, J. Ihm, M.L. Cohen, S.G. Louie, Calcium-decorated graphene-based nanostructures for hydrogen storage, Nano Lett. 10 (2010) 793–798.

[50] B. Kessler, Ç. Girit, A. Zettl, V. Bouchiat, Tunable superconducting phase transition in metal-decorated graphene sheets, Phys. Rev. Lett. 104 (2010) 047001.

[51] H. Zhang, C. Lazo, S. Blügel, S. Heinze, Y. Mokrousov, Electrically tunable quantum anomalous hall effect in graphene decorated by 5 d transition-metal adatoms, Phys. Rev. Lett. 108 (2012) 056802.

[52] M. Manadé, F. Viñes, F. Illas, Transition metal adatoms on graphene: a systematic density functional study, Carbon 95 (2015) 525–534.

[53] M. Sun, Q. Ren, Y. Zhao, J.-P. Chou, J. Yu, W. Tang, Electronic and magnetic properties of 4d series transition metal substituted graphene: a first-principles study, Carbon 120 (2017) 265–273.

[54] Y. Tang, H. Zhang, Z. Shen, M. Zhao, Y. Li, X. Dai, The electronic and diffusion properties of metal adatoms on graphene sheets: a first-principles study, RSC Adv. 7 (2017) 33208–33218.

[55] Z. Lu, S. Li, P. Lv, C. He, D. Ma, Z. Yang, First principles study on the interfacial properties of NM/graphdiyne (NM = Pd, Pt, Rh and Ir): the implications for nm growing, Appl. Surf. Sci. 360 (2016) 1–7.

[56] G. Kresse, J. Furthmüller, Efficiency of ab-initio total energy calculations for metals and semiconductors using a plane-wave basis set, Comput. Mater. Sci. 6 (1996) 15–50.

[57] G. Kresse, J. Furthmuller, Phys. Rev. B 54 (1996) 11169.

[58] G. Kresse, D. Joubert, From ultrasoft pseudopotentials to the projector augmented-wave method, Phys. Rev. B 59 (1999) 1758.

[59] H.J. Monkhorst, J.D. Pack, Special points for Brillouin-zone integrations, Phys. Rev. B 13 (1976) 5188.

[60] X. Lin, J. Ni, Electronic and magnetic properties of substitutionally Fe-, Co-, and Ni-doped BC$_3$ honeycomb structure, J. Appl. Phys. 111 (2012) 034309.